LANGMUIR

pubs.acs.org/Langmuir Article

Ligand Interactions and Nanoparticle Shapes Guide the Pathways toward Interfacial Self-Assembly

U. Gupta and F. A. Escobedo*

Cite This: *Langmuir* 2022, 38, 1738−1747 Read Online

ACCESS | Metrics & More | Article Recommendations | Supporting Information

ABSTRACT: Non-equilibrium molecular dynamics simulations are used to probe the driving forces behind the formation of highly ordered, epitaxially connected superlattices of polyhedral-shaped nanoparticles (NPs) at fluid−fluid interfaces. By explicitly modeling coarse-grained ligands that cap the NP surface, it is shown that differences in NP shapes and time-dependent facet-specific ligand densities give rise to drastically different transformation mechanisms. Our results indicate that the extent of screening of the inter-particle interactions by the surrounding solvation environment has a significant impact on reversibility and ultimately the coherence of the final two-dimensional superlattice obtained. For the particle shapes examined, a hexagonal pre-assembly and a square superlattice final assembly (upon preferential ligand desorption from {100} facets) were prevalent; however, cuboctahedral NPs formed intermediate epitaxially bonded branched clusters, which eventually grew and rearranged into a square lattice; in contrast, truncated octahedral NPs exhibited an abrupt rhombic-to-square transition driven by the clustering of their numerous {111}-ligands that favored the stacking of linear NP rods. To track the incipient order in the system, we also outline a set of novel order parameters that measure the local orientation alignment between nearest-neighbor pairs. The simulation protocols advanced in this work could pave the way forward for exploration of the vast phase space associated with the interfacial self-assembly of NPs.

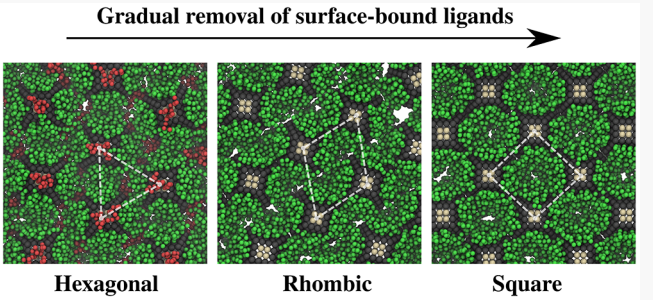

1. INTRODUCTION

Recent studies have made great strides in perfecting the synthesis protocols of not only faceted colloidal nanoparticles[1,2] (NPs) but also of the wide range of superlattice structures that emerge from them. Remarkably, these superstructures have been shown to possess long-range order and coherence across micron length scales. These discoveries have poised colloidal NPs as a promising candidate for the next generation of electronic materials[3,4] with applications in optics[5−7] and photovoltaics.[8−10] This has also spurred numerous experimental and computational studies that attempt to shed light on the underlying thermodynamic and kinetic processes driving the phase changes associated with superlattice formation.

The fundamental step driving the self-assembly process of truncated-cube shaped (octahedral symmetry) NPs is the formation of an irreversible epitaxial connection between the exposed {100} facets of two colloidal NPs.[11−15] Indeed, the {100} facets are reported to be relatively much more "sticky" when compared to the other major NP facets, for example, {111}. In practice, to prevent premature, uncoordinated inter-NP bonding, the NP surfaces are initially protected by binding ligands to them. The self-assembly process is therefore divided into two major sequential steps. First, ligand-covered NPs aggregate at a fluid−fluid interface to form a "pre-assembled" structure. This pre-assembly, held together by stabilizing inter-NP ligand interactions, is allowed to equilibrate. Subsequently, through the introduction of a chemical trigger[16] (typically ethylenediamine or EDA), the surface-bound ligands are desorbed, leading to exposed NP facets. The NPs can then fuse to form epitaxial bonds, and the pre-assembled structure can undergo transformation into the final connected superlattice structure.

In previous work,[17,18] the local density of NPs was indirectly constrained by changing the simulation box size for a given number of NPs, and the long-range interactions due to ligands were coarse-grained by encoding them directly into the NP surface beads. However, during experimental synthesis, the unconnected ligand-passivated NPs are held together in a "pre-assembled" state through ligand−ligand interactions. Moreover, as we demonstrate in Section 3.1, the potential-of-mean-force (PMF) landscape as a function of inter-NP is a complex function of ligand coverage. As surface-bound ligands are gradually desorbed away, the free-energy (FE) minimum changes continuously from a relatively large inter-NP distance to the

Received: October 20, 2021
Revised: January 16, 2022
Published: January 27, 2022

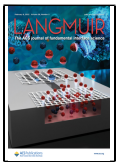

https://doi.org/10.1021/acs.langmuir.1c02804
Langmuir 2022, 38, 1738−1747

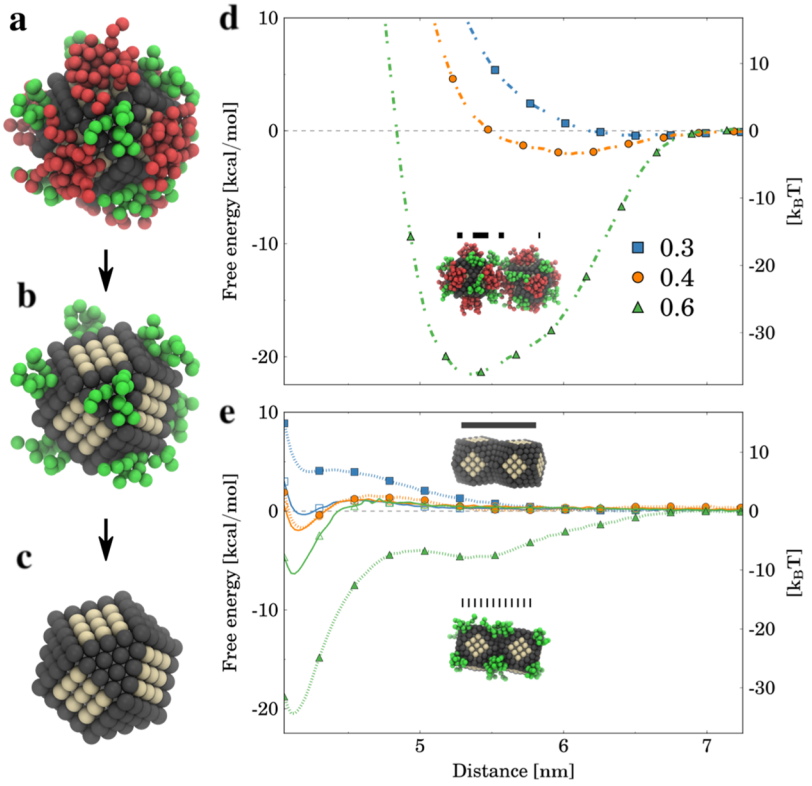

Figure 1. (a) Coarse-grained, polybead representation of the NP core fully covered by ligands. As the reaction progresses, the {100} facet-bound ligands (red beads) are gradually desorbed, relatively fast leading to the (b) intermediate state where only the {111}-facets are (almost) fully ligand covered, whereas the {100}-facets are completely bare. The "sticky" exposed {100}-facets (white) form the inter-NP epitaxial connections. (c) Desorption of the {111}-bound ligands, taking place over a much longer time scale, leaves bare the NP core. The gray beads make up both the edges, and the {111}-facets, and are modeled as purely repulsive. (d,e) PMF for a pair of CO-shaped NPs, with an edge size of 3.1 nm. (d) Dash-dotted line represents the PMF of fully covered NPs [as shown in (a), left inset] for different solvent parameters (s). (e) Similarly, the dotted and solid lines represent the PMF of only {111}-covered [(b), right inset] and completely bare NPs [(c), left inset], respectively. All ligand types are functionally the same but are colored differently to distinguish between the tethering facets.

distance where the bare {100}-facets of NPs are in contact. This change is ultimately observed in the form of a reduction in lattice spacing with time. By modeling the explicit ligands, their stochastic removal, and the overall densification of domains, we strive, in this work, to achieve a more realistic description of NP surface deprotection and the resulting structural evolution of multi-NP systems. Our results show that addition of these details has a major effect on the transformation mechanisms for the various experimentally observed phases.

In recent years, various mechanisms have been proposed for the formation of multi-layer NP assemblies.[15,19−23] Whitham and Hanrath[15] proposed that this transformation occurs at coherent grain boundaries through distinct nucleation and growth steps. Similar efforts have been made to elucidate the quasi-2D NP self-assembly under interfacial confinement.[24−26] Geuchies et al.[26] proposed a formation mechanism for the final square superlattice via a pseudo-hexagonal intermediate, facilitated by the increased attraction between bare {100} facets. In Section 3.2, with the use of molecular dynamics (MD) simulations, we demonstrate that our coarse-grained model can reproduce the experimentally observed square phase. More importantly, we observe that based on the choice of NP shapes and density of the capping ligands bound to the NP surface, the transformation from a hexagonal, unconnected lattice to a an epitaxially connected square lattice can occur through different pathways. In particular, for the cuboctahedron (CO) shape, the phase change proceeds by a stepwise growth mechanism. This involves the formation of multiple, small, branched clusters, which then rearrange to form bigger clusters. However, for the truncated octahedron (TO) shape, a highly concerted transformation is observed via an intermediate rhombic phase, which is composed of linearly stacked rods.

The rest of this paper is organized as follows. In Section 2, we describe the model and simulation methods employed, including a description of the order parameters introduced for later analysis. In Section 3, we present the main results of our study, and in Section 4, we provide some concluding remarks and an outlook for future work.

2. METHODS

2.1. NP Model. We use a polybead[17,20,27,28] model to describe faceted, hollow NPs, as illustrated in Figure 1c. The simulations are run using MD[29] software. The MARTINI[20,30] force-field is used to model inter-species interactions (as detailed in the Supporting Information). Instead of using the surface beads as coarse-grained representations of the ligand−ligand interactions, we explicitly model fully flexible, five-bead ligands to represent C-18 oleate ligands. Ligands are bound to the surface beads on the {100} [represented by red beads in Figure 1a] and {111} (green beads) facets using harmonic bonds. Consistent with the experimental findings, we allow inter-NP epitaxial connections through the {100} facets only. Therefore, only the surface beads belonging to the {100}-facets (white beads, as shown in Figure 1) interact through a cut and shifted Lennard-Jones potential, while the rest of the surface beads (gray) are purely repulsive (as detailed in the Supporting Information). This is also justified by the fact that, in this work, in the window of simulated conditions and reported transitions, the {111}

https://doi.org/10.1021/acs.langmuir.1c02804
Langmuir 2022, 38, 1738−1747

facets are almost always fully ligand bound. Therefore, the presence of attractive forces on these surfaces has a negligible effect on the observed self-assembly dynamics. The Lennard-Jones interactions on the NP surface are primarily meant to provide steric hindrance (to preclude penetration into the NP core) and enact short-range attraction associated with epitaxial bonds.[17,18,20] During experimental synthesis of PbX NPs, the chemisorption of the oleate ligands onto the NP causes an enlargement of the {111} facets at the expense of {110} facets, often giving rise to shapes ranging from CO to TO.[31] Therefore, in this work, we focus on two representative NP shapes: CO with five beads per edge ($e = 5$) and TO with $e = 4$. Moreover, the transition from CO to TO involves a reduced {100} area, which translates into smaller energy per {100}-epitaxial connection. This is accompanied by a corresponding increase in {111} area, which translates into a much larger number of binding sites for oleate ligands. Therefore, these two shapes, while being representative of the experimentally observed shapes, also provide an excellent opportunity to compare the role of {111}-ligands in the formation of the square phase. The effect of solvation of the ligand shell in the surrounding fluid is captured by a solvent parameter, s. This parameter scales the attractive part of the standard 12-6 Lennard-Jones potential to account for the effect of screening of inter-species interactions by the surrounding solvent.[20]

MD simulations were conducted for up to 144 NPs (comprising between 75,000 and 165,000 coarse-grained beads) whose concentration was controlled as follows. In typical experiments, large concentration fluctuations occur over the interface, which lead to both dense and sparse regions of NPs, in part driven by the loss of ligands and the concomitant reduction of NP footprint area; it is only the dense regions which are of interest for interfacial self-assembly. Because of the limited ability to simulate only a small number of NPs, the dense NP regions would be uncharacteristically small and disconnected if simulated in a canonical ensemble with constant interfacial area. Hence, to form larger, more representative dense NP regions, we implemented an isobaric ensemble. This allows for a reduction in the total interfacial area, and therefore an increase in the NP concentration, by squeezing out regions left empty by the loss of NP footprint area during the ligand deprotection process. The osmotic pressure was small ($P = 1$ atm) and was merely intended to keep a compact interfacial packing of the NPs with or without ligands.

To minimize the computational cost associated with simulating the surrounding solvent, we use an implicit solvent description implemented through a Langevin thermostat. The effect of the fluid−fluid interface is captured by employing the recently developed quaternion-based orientation constraint (QOCO) scheme.[18] By applying suitable spring potentials to each NP, we can reproduce the positional and orientational preferences imposed by the interfacial confinement on each NP. In particular, we are interested in ethylene glycol (EG) interfaces where PbX NPs capped with oleate ligands have been shown to preferentially orient with their 100 axes parallel to the interface normal.[15,25,26] We emulate this preference using an orientation FE landscape previously reported[18] for a TO-like shape (as detailed in the Supporting Information). The position of the center-of-mass of each NP is allowed to fluctuate about the "vertical" direction normal to the interface using a harmonic spring. In this study, we limit ourselves to studying a baseline model case, where the two solvents making up the interface are not significantly different in their solvation quality with respect to the NP-ligand system. We hence use a uniform solvent parameter throughout the entire system, regardless of the location with respect to the interface.

Ligand-binding energy and surface coverage have been shown to be facet-specific, $E_{\{100\}} < E_{\{110\}} < E_{\{111\}}$, such that the surface deprotection is fastest for the {100} facet.[32] This trend is captured in our simulations by stochastic desorption of ligands from the NP facets.[33] The desorption is modeled by assuming first-order kinetics using a Poisson process

$$\Delta L_f = \frac{L_f}{L_{f,0}} = 1 - e^{-r_f t} \tag{1}$$

where ΔL_f is the fraction of ligands desorbed from facet f and r_f is the rate of ligand desorption from facet f. The reported value[34] of rate of desorption of amine-based ligands from NMR data is around 50 s^{-1}. However, for the time scales accessible in our simulation setup, we are restricted to use much faster rates, specifically $r_{\{100\}} = 5 \times \frac{10^{-5}}{10^3\ \mathrm{fs}} = 50\ \mu s^{-1}$, $r_{\{111\}} = 0.5\ \mu s^{-1}$. We also assume uniform concentration of the chemical trigger across the simulation box. For the length scales corresponding to our simulations (~100 nm), this assumption has been shown to be largely true for EDA as a chemical trigger in an EG sub-phase.[25] For specific cases intended to explore the effect of {111}-ligand removal, we change $r_{\{111\}}$ to 50 μs^{-1} once all {100}-ligands have been removed, to thus make the simulation temporally accessible. This assumption is justified based on the separation of the time scales of ligand exchange for different facets.[32]

2.2. Order Parameters. Owing to the quasi-2D nature of the system under consideration, we employ the 2D bond-orientation order parameter[35] as a measure of resemblance between the local environment around the ath NP (NP_a) and a perfect k-fold lattice

$$\psi^a_{k,n} = \frac{1}{n}\sum_{b=1}^{n} e^{ik\theta_{a,b}}\ \forall\ b \in \mathrm{NN}(a) \tag{2}$$

where $\mathrm{NN}(a)$ is the set of nearest neighbors of NP_a, n is the number of nearest neighbors that are accounted for, $\vec{\mathbf{r}}_{a,b}$ is the NP-pair vector drawn from the center-of-mass of NP_a to NP_b, and $\theta_{a,b}$ is the angle between $\vec{\mathbf{r}}_{a,b}$ and the positive x-axis. Typically, we only include the k-nearest neighbors ($n = k$), such that $\psi^a_{n,n} = \psi^a_n$ for simplicity. We then report the averaged, scalar, 2D bond-orientation order parameter $\psi_n = \langle|\psi^a_n|\rangle$ as a function of time. Additionally, the shifted and normalized box projection area $\Delta A_{\mathrm{box}} \in [0,1]$ is measured as

$$\Delta A_{\mathrm{box}} = \frac{A_{\mathrm{box}} - A_{\mathrm{Sq}}}{\max_{t=0}^{\infty}(A_{\mathrm{box}}) - A_{\mathrm{Sq}}} \tag{3}$$

where A_{box} is the area of projection of the simulation box along the interface normal and A_{Sq} ($\Delta A_{\mathrm{box}} = 0$) is the area of a perfect square lattice made from the NPs in the system. The denominator normalizes the box projection area for a given trajectory.

In general, the global orientation of the NP at a cylindrically symmetric planar interface can be defined by the intrinsic ($y-z'-y''$ coordinate convention) Euler angles (ϕ, θ, ψ). However, owing to their ease of interpretability in terms of the NP facets, the angles of the closest approach ($\alpha_{m,f}$, described in ref 18) provide a better descriptor of the NP orientation. $\alpha_{m,(hkl)}$ is the smallest rotation angle required to orient the NP crystallographic direction $\langle hkl\rangle$ along the interface normal. We specifically focus on three major crystallographic directions $\langle 100\rangle$, $\langle 110\rangle$, and $\langle 111\rangle$.

2.3. Pair-Alignment Parameter. Traditional bond order[36] (ψ_n, Q_n) and orientational order (P_n, I_n) parameters do not account for information about the particle anisotropy in tandem with the bond order. While we do calculate ψ_4 and ψ_6 in our systems to capture 2D square and hexagonal bonding symmetry, respectively, in this work, we further develop a generalized order parameter to quantify the alignment of a NP with respect to its nearest neighbors in 3D. Consider an arbitrary NP a and one of its nearest neighbors $b \in \mathrm{NN}(a)$. For an arbitrary NP_a, we define $\beta_{f,a}(b)$ as the angle of the closest alignment of its facet f, to the NP-pair vector, $\vec{\mathbf{r}}_{a,b}$

$$\beta_{f,a}(b) \in \left[0, \cos^{-1}\frac{1}{\sqrt{3}}\right]: \{a \in \mathbb{Z} | 1 \le a \le N;\ b \in \mathrm{NN}(a)\} \tag{4}$$

The pair-alignment parameter is similar to the angle of the closest approach, $\alpha_{m,(hkl)}$ as described in the previous section in all aspects except that the direction of alignment is changed from a global-fixed interface normal to a dynamically changing local NP-pair vector. A detailed treatment on the calculation of the angle of the closest approach is presented elsewhere.[18] Additional details about the pair-alignment parameter can be found in the Supporting Information and Movie S1.

https://doi.org/10.1021/acs.langmuir.1c02804
Langmuir 2022, 38, 1738−1747

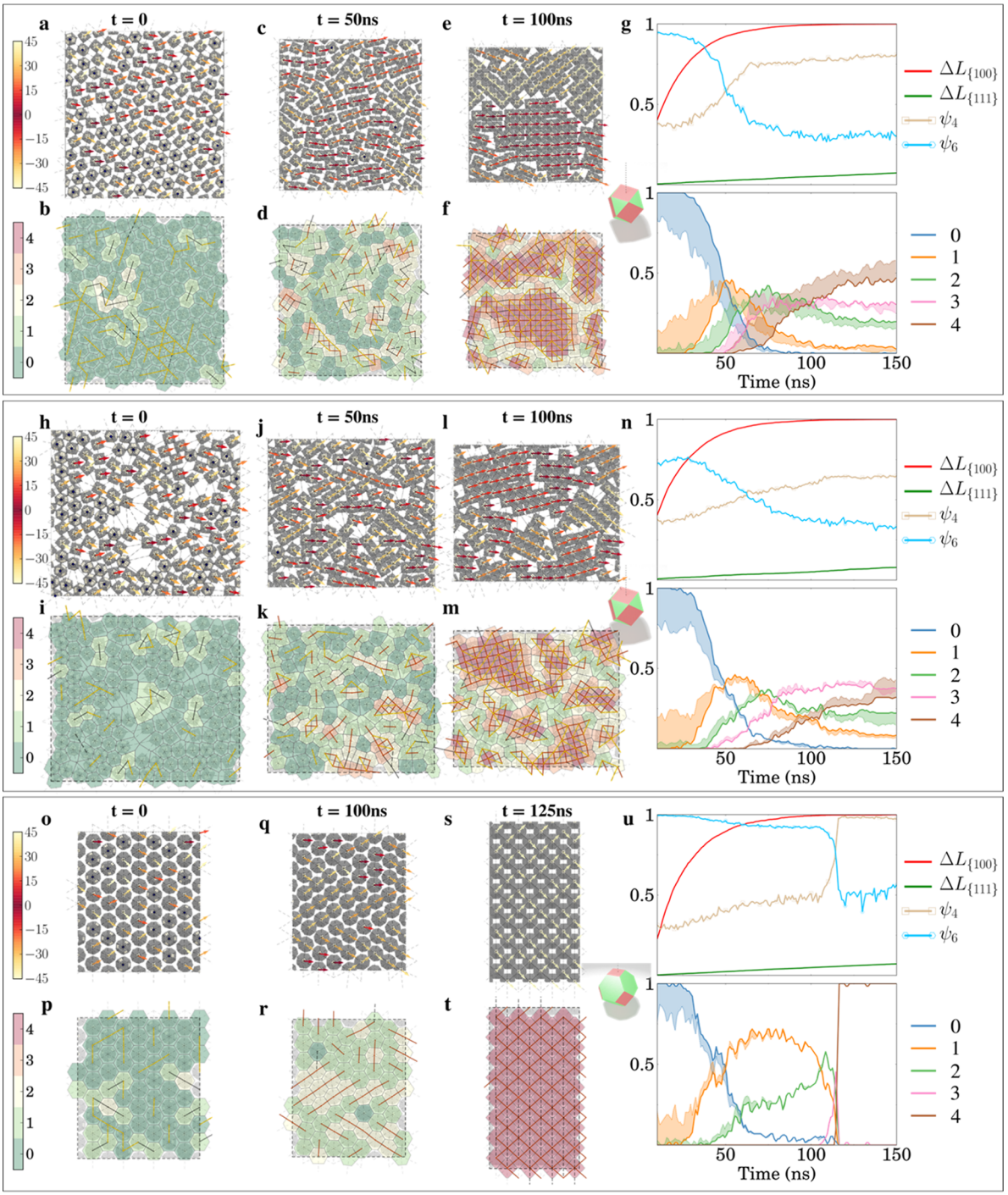

Figure 2. Representative trajectories for the selected cases illustrating different assembly mechanisms. (a−g) Kinetics of self-assembly of 144 CO NPs (cartoon illustration in the inset) in a relatively good (implicit) solvent (s = 0.4). Each column in (a−f) represents a simulation timestamp (0, 50, and 100 ns). The top row shows MD snapshots, viewed along the interface normal. For each NP oriented with their ⟨100⟩ axis parallel (within 10°) to the interface normal, its in-plane orientation is shown using an arrow color-coded (color bar on the top left) from red (aligned to the box x-axis) to white (45° from the box x-axis). For other orientations, the NP center is marked by a blue dot. The bottom row shows the respective Voronoi diagrams with each cell colored according to number of {100}-epitaxially connected nearest-neighbor pairs from 0 (green) to 4 (red). Additionally, the {100}-epitaxially connected and {100}-aligned pairs are joined, respectively, by red and black overlaid solid lines. Similarly, the {110}-connected and {110}-aligned pairs are joined, respectively, by yellow solid and thick black dashed lines. Plots in (g) summarize the time evolution of various order parameters, tracking the transformation (see the main text): the top plot shows the fraction of ligands desorbed from facet f, ΔL_f, and ψ_4, ψ_6 and the box projection area, A_{box}; the bottom plot shows the epitaxial $f_{ep,k}$ (solid line) and alignment $f_{al,k}$ $\forall$ $k \in \{0,1,2,3,4\}$ (dotted) correlations. A similar layout as (a−g) is shown in (h−n) for the self-assembly for 144 CO NPs in a relatively poor solvent (s = 0.6) and in (o−u) for 64 TO NPs with a good solvent (s = 0.4).

https://doi.org/10.1021/acs.langmuir.1c02804
Langmuir 2022, 38, 1738−1747

Furthermore, we can classify a nearest-neighbor pair based on the individual pair alignments of its constituents. We define a nearest-neighbor (a,b) pair as f-aligned if

$$(\beta_{f,a}(b) < \beta_0) \wedge (\beta_{f,b}(a) < \beta_0) \tag{5}$$

where β_0 is a threshold value (typically 10°). We thus identify the NN-pairs that are {100}-aligned but not necessarily epitaxially connected. With that we can define the fraction of NPs with exactly k {100}-aligned pairs as

$$f_{al,k}{:}k \in \{0, 1, 2, 3, 4\}\text{s. t.} \sum_{k=0}^{4} f_{al,k} = 1 \tag{6}$$

As a precursor to the actual epitaxial bond, this parameter tracks the local (in the first-nearest-neighbor shell) alignment changes as a measure of the incipient order in the system.

We can also identify the NN-pairs that are epitaxially connected. We define a nearest-neighbor (a,b) pair as f-connected if

$$(\beta_{f,a}(b) < \beta_0) \wedge (\beta_{f,b}(a) < \beta_0) \wedge (|\vec{\mathbf{r}}_{a,b}| < r_0) \tag{7}$$

This stronger classification includes a distance cut-off to ensure that the NPs in the f-aligned pair also lie within a distance, r_0, such that the f-facets of both NPs can come into contact. In a similar fashion, we define the fraction of NPs with exactly k {100}-epitaxial connections as

$$f_{ep,k}{:}k \in \{0, 1, 2, 3, 4\}\text{s. t.} \sum_{k=0}^{4} f_{ep,k} = 1 \tag{8}$$

For a perfect, infinite square lattice, $f_{ep,4} = 1$. The $f_{ep,4}$ correlations can be used as an alternate order parameter (that captures square symmetry like ψ_4) for shapes with octahedral symmetry confined to two dimensions. The reason for considering only up to the first four ($k \leq 4$) correlations is because (1) the {100} facets have an octahedral symmetry, and (2) we only consider the case of formation of monolayer superlattices. In other words, by restricting the NPs to a quasi-2D interfacial region, we effectively enforce that a given NP can have a maximum of 4 {100} facets accessible for epitaxial contacts (parallel surface-to-surface) in the interfacial plane. This happens when the NP is oriented with its ⟨100⟩ facet normal along the interface normal. If, however, the NPs are allowed to fluctuate more about the interfacial plane, then they can form epitaxial connections through all six {100} facets, leading to multi-layer structures.

3. RESULTS AND DISCUSSION

We design our simulation protocol to mimic the effects and trends associated with experimental processing conditions. Accordingly, the {100}-bound ligands are removed gradually (at $r_{\{100\}} = 50\ \mu s^{-1}$) without significantly desorbing the {111}-bound ligands ($r_{\{111\}} = 0.5\ \mu s^{-1}$). As the driver of the sought-after change, the fraction of ligands desorbed from facet f, ΔL_f, is depicted as a function of time in the top plot of Figure 2g,n,u.

3.1. Effect of the Solvent. The quality of the solvent is tuned by the solvent parameter s. A higher value implies poor screening of inter-species interactions by the solvent resulting in lower (more negative) energies of interaction (as detailed in the Supporting Information) between all species and vice-versa. A value of $s = 0$ implies complete screening and good solvent conditions, whereas $s = 1$ represents interactions in vacuum, akin to poor solvent conditions. To illustrate this, we calculate the PMF between two CO NPs in different implicit solvent environments using an umbrella sampling approach.[28,37] One consequence of improving the solvent quality is the swelling of the ligand shell. This can be seen in the increasing equilibrium "contact" distance (corresponding to a minimum in the PMF) between the fully ligand-covered NPs (as illustrated in Figure 1a), with increasing s (Figure 1d). As the deprotection reaction progresses, the {100}-bound ligands are gradually removed, eventually rendering the {100} facets bare (Figure 1b). For this scenario, the PMF landscape is changed drastically, and the particles contact at closer distances (Figure 1e, dotted lines). For each profile, we also observe a relatively shallow, local minimum at the separation corresponding to interactions between the {111}-ligand shells of the two NPs. As expected, we observe a second minimum that represents the epitaxial bond between the {100}-facets.

While it is true that using a relatively poor solvent would lead to an overall stronger inter-NP interaction ($s = 0.6$, dotted green line), in practice, we find that it also leads to premature sticking of the pre-assembled structure. In this situation, even 1−2 neighbors can provide enough stability ($10-15k_BT$), that cannot effectively be overcome by thermal energy. This leads to irreversible sticking between ligand shells, thereby preventing the equilibration of NP positions and orientations and promoting the formation of localized metastable clusters filled with defects. A very good solvent ($s < 0.4$), on the other hand, would screen all inter-ligand interactions and therefore provide no energetic incentive for the formation of a pre-assembled structure. In such a scenario, the NPs would require an external force to bring them together (such as an osmotic pressure, as discussed in Section 2.1).

We note that an alternate physical interpretation of the solvent parameter is the extent of solvent evaporation, as explored by Fan and Grünwald.[20] This interpretation is motivated by the fact that removal of the solvent by evaporation also results in stronger inter-ligand interactions and more compact ligand shells. In fact, a more reversible, coherent self-assembly is achieved experimentally using a smaller evaporation rate.[38−40] In our simulations, we use a fixed value of the solvent parameter for a given trajectory, to primarily probe the effect of the solvent environment on the kinetics of structure transformation.

In the limit of complete deprotection of the {111}-facets by ligand removal, the bare NPs form a stable {100}−{100} epitaxial bond (Figure 1e, solid lines). We note that using the MARTINI parameters (as detailed in the Supporting Information), the energy of contact (Figure 1e, solid lines) between two {100}-facets at full epitaxial contact is $O(10^1)k_BT$ [that is, $O(10^1)$ kcal/mol or $O(10^{-19})$ J]. This is in line with previous reports for corresponding values for {100} facets in PbX NPs.[17,41] The presence of {111}-ligands appreciably changes the PMF, as compared to that for bare NPs (Figure 1e dotted and solid lines, respectively). For a good solvent, due to the screening effect of the solvent, the enthalpic incentive of epitaxial bond formation and ligand−ligand interactions is overshadowed by the strong entropic penalty incurred by compression of the ligand shells. For a poor solvent, on the other hand, the PMF profile is dominated by the strong enthalpic attraction associated with (1) the formation of the epitaxial bond and (2) increased ligand−ligand interactions. Finally, a comparison between the PMFs of fully ligand-passivated (Figure 1d) and bare NPs (Figure 1e, solid lines) shows that the interactions between fully covered NPs of the given size range are dominated by ligand−ligand interactions.[20]

3.2. General Trends. Despite displaying two distinct transformation mechanisms, both NP shapes under consideration, namely CO and TO, eventually assemble into a square lattice bound by {100}-epitaxial connections. In general, due to the nature of the imposed orientational behavior [⟨100⟩ axis parallel to the interface normal, as described in Section 2.1], the

https://doi.org/10.1021/acs.langmuir.1c02804
Langmuir 2022, 38, 1738−1747

initial equilibrated pre-assembled structures have a majority of NPs oriented with their ⟨100⟩ axes parallel to the interface normal. Owing to a relatively small barrier between the {100}-up and {111}-up configurations in the underlying PMF (as detailed in the Supporting Information), a significant fraction of NPs orients with their ⟨111⟩ parallel to the interface normal. These fully ligand-covered NPs, oriented with {111}-up, show a strong tendency for pair-alignment with their {110}-facets. This is attributed to the fact that, for NPs trapped at the interface, the {111}-up orientation favors sixfold ligand-mediated binding with neighbor NPs on the interfacial plane, that is, the ligands bind to six (out of a total of eight) {111} facets and to all six {100} facets and are made available for inter-NP interactions. Therefore, an increased inter-particle ligand−ligand coordination is made possible in a quasi-2D hexagonal packing with a {111}-up orientation. This is also seen in a relatively high initial value of the fraction of {110}-aligned pairs in the 6-NN (as detailed in the Supporting Information) and a six-fold distribution of the {110}-aligned pairs visualized as yellow lines overlaid on the Voronoi diagrams in Figure 2.

3.3. Cuboctahedron. We now consider the contrasting cases of assembly of 144 CO NPs in a well-solvated (s = 0.4, Figure 2a−g) and a poorly solvated environment (s = 0.6, Figure 2h−n). As discussed in Section 3.1, pre-assembly in a relatively poor solvent is fraught with large void volumes (Figure 2h) in contrast to the relatively well-equilibrated, close-packed distribution for s = 0.4 (Figure 2a). This fact is also reflected in the difference of the initial ψ_6 values. Also, since the {100}-facets are initially fully covered by ligands, there are no epitaxial connections, that is, $f_{ep,0}$ = 1. However, a significant fraction (15−20%) of the NPs displays a {100}-alignment with their nearest neighbors without being connected with an epitaxial bond. This is quantified in terms of the difference $f_{ep,n} - f_{al,n}$ between the bonding and alignment correlations [shaded regions in the respective bottom plots of Figure 2g,n].

With the gradual removal of the {100}-bound ligands, the mutually exposed {100} facets in NN-pairs begin to bond. With the appearance of NP "dimers,"[42] $f_{ep,1} \neq 0$, there is a corresponding fall in the fraction of free "monomers," $f_{ep,0}$. Initially, no NPs are found with more than one epitaxial connection, that is, $f_{ep,k} = 0\ \forall\ k \in \{2,3,4\}$. It is only after the fraction of dimers reaches an appreciable value that the fraction of trimers starts to increase, resulting in the formation of both I-shaped (parallel bonds) and L-shaped (perpendicular bonds) clusters. The fall of the initial, high sixfold order is highly correlated with the appearance of NP "trimers." The increase in order in the system is stepwise and not continuous as each subsequent $f_{ep,n}$ correlation only emerges after the previous correlation $f_{ep,n-1}$ and increases to a certain point (Figure 2g,n). Ideally, if the final structure was a single, continuous lattice, then the correlations $f_{ep,k}\ \forall\ k \in \{0,1,2,3\}$ would decay to zero, while the ultimate value of $f_{ep,4}$ would remain high.

Interestingly, in a good solvent environment, changes in alignment occur in the neighborhood of the NPs before the formation of an epitaxial bond. All bonding correlations ($f_{ep,n}$) emerge, after a small delay, once the local alignments ($f_{al,n}$) take place. This delay is visualized in terms of the larger thickness of the shaded regions in Figure 2g, as compared to that for a poor solvent, as shown in Figure 2n. The existence of this delay has two major implications: (1) the screening effect provided by the solvent helps prevent premature inter-NP bonding, and (2) formation of epitaxial bonds introduces local alignment changes to the NP neighborhood, which are then propagated into further epitaxial bonds. For a poorly solvated system, this delay is rather short, which translates into insufficient equilibration time and the formation of fast, irreversible epitaxial bonds that preclude the concerted changes observed for the well-solvated case. This causes the emergence of multiple small domains, which are rotated with respect to each other and give a weaker fourfold order, as seen in the relatively small values of ψ_4 and $f_{ep,4}$.

3.4. Truncated Octahedron. We now consider the assembly of 64 TO NPs in a well-solvated medium (s = 0.4, Figure 2o−u). The observed transition path can be divided into two distinct parts. Like the transformation seen in CO, with the removal of the {100}-bound ligands, the initial emergence of "dimers" is observed. Thereafter, an increase in $f_{ep,2}$ is driven exclusively by the formation of linear rods—a result of two parallel {100}-epitaxial connections. This is a direct consequence of the greater stability of the initial sixfold symmetry (high ψ_6), which does not break down by the formation of epitaxial bonds (Figure 2u). The formation of branching (L-shaped clusters) would in principle induce local fourfold order, as observed for the CO shape. However, due to the formation of the linear rods, the hexagonal unit cell gradually shifts to a rhombic one. This stable rhombic structure is held together by the larger number of {111}-ligands for TO, as compared to CO. We also note that for a TO (with edge $e \geq 2$), the number of beads per close-packed, hexagonal {111} facet $[3(e-1)(e-2) + 1]$ is greater than that per square-packed, square {100} facet $[(e-2)^2]$. Eventually, the rods shift with respect to each other by a distance equal to half the lattice parameter for a perfect {100}-connected square lattice, giving rise to a "stacked rods" phase (Figure 2q,r).

For a fraction of the observed trajectories, the system remains stuck in this "stacked rods" configuration described above. However, in some cases, the system spontaneously and abruptly transitions from this phase to the square phase. The transformation is brought about by a concerted sliding of the rods relative to each other. This is marked by a sharp transition in the various order parameters, for example, an abrupt increase in ψ_4 and $f_{ep,4}$ with a correlated decrease in ψ_6 and $f_{ep,2}$ (Figure 2u). Expectedly, for the cases where the system gets stuck in the "stacked rods" phase, a subsequent gradual removal of the {111}-ligands leads to breaking of the sixfold symmetry, causing it to sharply transition into the square phase. This phase change is also accompanied by a change in the box shape and a significant decrease in the area of the system, A_{box}. Since $\Delta A_{box} < 0$ for the transition, increasing the pressure would also tend to favor the transition. This coordinated sliding of rods is reminiscent of the displacive (Martensitic) transformations observed in intermetallic alloys.[43] This process can be visualized in Movies S2 and S3 of the Supporting Information.

By virtue of their longer persistence on the NP surface, {111}-ligands stabilize and hold the hexagonal bond order and enable the formation of the linear rods. Interestingly, such structures are stabilized by the formation of a serpentine network composed of {111}-ligands (see Figure 3b). These serpentine moieties are localized between any two adjacent rods. In this configuration, each NP on average gains $\sim 40 k_B T$ of stabilizing energy by the inter-{111}-ligand interactions alone, when compared to the hexagonally distributed, unconnected configuration of the pre-assembly [see Figure 3e]. In some cases, as these ligands gradually desorb, the thermal energy eventually becomes sufficient to cause a concerted phase change into the square lattice. At this stage, the {111}-ligands can drive the sliding of these rods to reduce the global energy of the interaction between

https://doi.org/10.1021/acs.langmuir.1c02804
Langmuir 2022, 38, 1738−1747

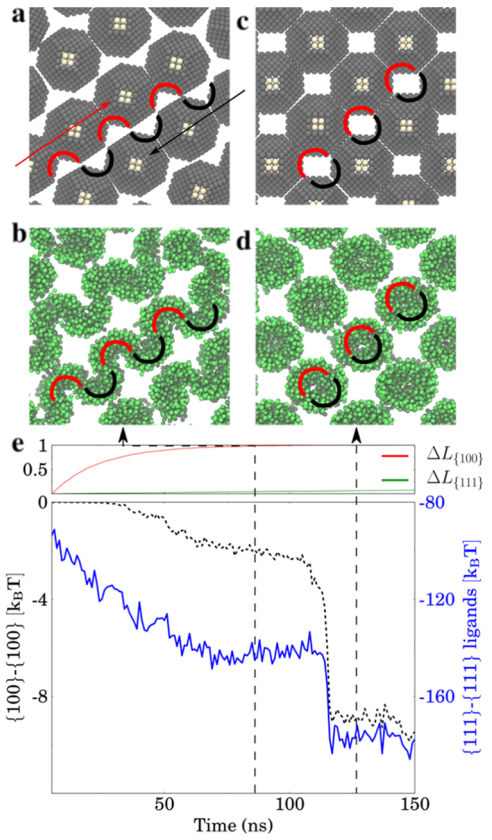

Figure 3. (a−d) Close-up snapshots from the simulation of 64 TO NPs in a relatively good solvent (s = 0.4), as depicted in Figure 2o−u, corresponding to different timepoints. The "stacked rods" phase depicting (a) only the TO NP-core beads and (b) only the {111}-ligand beads. This phase is stabilized by the formation of isolated serpentine networks, made up of {111}-ligand contacts, between adjacent rods. The average conformation of {111}-ligands (between two epitaxially connected NPs) for the top-left and bottom-right rods is depicted by red and black semicircles, respectively. (c,d) Eventually, the rods slide past each other to form the square phase, while the {111}-ligands change from the serpentine to cylindrical blob-like clusters. (e) Top plot tracks reaction progress in terms of extent of ligand removal from the {100} (in red) and {111} (in green) facets. The bottom (e) plot depicts the energy of epitaxial bond (black, dotted) and energy of interaction between the {111}-ligands (blue, solid) per NP, on average, in k_BT units; the phases shown in (a,b) and (c,d) correspond to the points marked by the left and right, vertical dashed lines, respectively.

the {111}-ligand beads (Figure 3e). This is because in the square phase, in addition to the formation of two additional, stabilizing {100}-epitaxial bonds per NP, each square inter-NP interstice "void" is filled with ligands bound to 2 {111}-facets each from four different NPs. The {111}-ligands take on a blob-like conformation, when localized in such voids, as visualized in Figure 3d. The serpentine-to-blob transformation (as featured in Movies S3 and S4 in the Supporting Information) can be explained in terms of the large, correlated drop in the energy of interactions between the {111}-ligand beads, which amounts up to $40k_BT$ per NP. In contrast, the stability gained, by the increased interactions between the {100} facet beads, is an order of magnitude smaller ($\sim 4k_BT$). In this way, {111}-ligands play a dominant role in mediating the orthorhombic to square transformation via the formation of an intermediate "stacked rod" phase. It is interesting to note that the sliding process also induces a slight, overall rotation in the superlattice directions (notice the difference between the initial and final orientations in Figure 3a,c respectively and also Movie S2 in the Supporting Information).

Due to the kinetic nature of the assembly process (which would be more appropriately described by a transition path ensemble in a future study), in some trajectories, the transformation from the "stacked rods" to the square phase is not as dramatic as for the "affine" deformation shown in Figure 2o−u, which occurred in about 4 out of 15 replicate runs. Instead, it manifests as the transformation—through the sliding mechanism—occurring for only a portion of the simulation box, while the rest of the box remains stuck in the "stacked rods" phase. Expectedly, for these non-affine transformation trajectories, the change in the box size is not as pronounced (as detailed in the Supporting Information). Unlike the case of the CO shape, the local transformations still occur in a concerted fashion, mediated by the ligand−ligand interactions. Finally, using poorer solvents (i.e., by increasing s) has a similar effect—of creating disjoint, localized, and ordered clusters—to the CO shape.

Why do we observe such vastly different transition pathways for the two similar sized but differently shaped NPs? We address these differences from an energetic perspective. Recall that the CO-shaped NPs have a relatively smaller {111} and a correspondingly larger {100} facet area. This also results in fewer {111}- and more {100}-bound ligands. Owing to the relatively large area of {100} facets for CO, the energy per epitaxial bond is higher than that for TO. This, combined with the effect of faster desorption kinetics of the {100}-bound ligands, promotes more substantial {100}-epitaxial bonding in the CO's vicinity. This leads to the formation of L-shaped clusters, thereby inducing fourfold symmetry in the system. Breaking of the sixfold symmetry during the early stages of the process inhibits the formation of larger clusters via concerted processes. Larger clusters are eventually formed by the reorganization of smaller clusters. On the flip side, for the TO, the smaller incentive for the formation of {100}-epitaxial bonds along with the numerous {111}-ligands promotes the formation of linear structures. As demonstrated above, the {111}-ligands enhance favorable energetic contacts by forming serpentine networks in the NP interstitial spaces, leading to a "stacked rods" phase. In this way, the presence of {111}-ligands smoothly guides the system from a hexagonal to a square phase, via an intermediate pseudohexagonal phase. Moreover, the pointed {110} facets of the CO shape create a jagged interface between different small-sized clusters, which makes the self-assembly for the CO NPs more difficult than that for TO. Indeed, the CO {110} facets sterically prevent re-organization through sliding between different clusters. The TO shape, on the other hand, has more rounded {110} facets (edges instead of vertices).

4. CONCLUSIONS

In this work, we have probed the self-assembly of faceted, colloidal NPs under interfacial confinement. To aid the analysis, we also developed order parameters that describe the emergence of incipient local order in terms of generalized pair-alignment parameters. We show that with explicit coarse-grained ligands, our model and analysis tools are able to capture key aspects of the self-assembly process. We observed that CO-shaped NPs assemble via the formation of intermediate branched clusters with 1, 2, 3 {100}-epitaxial connections. However, the breaking of local sixfold order induced by the formation of proximal, L-shaped epitaxial bond-pairs initially inhibits the formation of

https://doi.org/10.1021/acs.langmuir.1c02804
Langmuir 2022, 38, 1738−1747

bigger clusters. Eventually, these smaller clusters rearrange to form the final square lattice. For the TO shape, this hexagonal to square transformation is mediated by the {111} surface-bound ligands through an intermediate phase made of linear, stacked rods that has a quasi-hexagonal bond order. During this assembly, typically no L-shaped branching emerges until the abrupt rhombic to square transition. We note that while changes from hexagonal to square structures have been experimentally observed in interfacial NP assemblies,[15,25] the precise intermediate structures and pathways predicted here have not.

We also demonstrated a direct correlation between the solvent quality and the degree of reversibility of inter-NP contacts at various stages of the assembly. An alternate interpretation of the solvent-quality parameter is as the extent of the evaporated solvent.[20] Therefore, one can argue that a faster rate of evaporation of the solvent could also explain the formation of irreversible defects, as described for the case of a poor solvent. We have employed an isobaric ensemble to ensure that, as ligands are gradually removed, the projection of the simulation box on the interfacial plane shrinks to eliminate the void area and promote the well-packed structures of larger clusters despite the small system sizes being accessible to our simulation. In this way, the laterally applied osmotic pressure is intended to mimic the moving boundary of a much larger transformation.

A similar effect (to changing the solvent quality or the evaporation rate) of altering the inter-NP binding free energy could be achieved by tuning the ligand chemistry directly. However, the choice of physical parameters like solvents or ligand chemistry is heavily constrained by the experimental setup, the choice of NP compound, and so forth. Inspired by our findings, we suggest an alternate experimental protocol that maintains close inter-NP contacts in the NP pre-assembly stage. Instead of using a strong enthalpic attraction between ligand shells, the pre-assembly can be driven and maintained by a small external lateral pressure that constrains and "compresses" the interfacial area. In this scenario, if the inter-NP contacts are designed to be sufficiently reversible (i.e., order of most a few k_BT), then the formation of defects will likely be minimized. This protocol can potentially be realized experimentally using, for example, a Langmuir Trough.[44,45] One potential limitation of the current formulation is the range of values that the solvent parameter can take on for the system to remain physically relevant. Consider, for example, the PMF for a pair of NPs in a very good solvent, $s = 0.3$ (Figure 1e, blue squares). For completely bare NPs (solid lines), the epitaxially bonded state, while favorable, has a very shallow well-representing reversible contact. Physically however, regardless of the quality of the surrounding solvent, epitaxial bonding entails the formation of irreversible, strong covalent and ionic bonds. A very good solvent only lowers the chances of NP facets coming together in the first place, and this is reflected in the modeled PMF. In the current study, we only consider cases ($s \geq 0.4$) where epitaxial attachment leads, with high probability, to effectively irreversible bonds between {100} facets. Accordingly, we expect that the main results and trends in behavior reported in this work will not be significantly affected by the specific strength of the modelled epitaxial bonds. In future studies, this formulation could be updated to account for the large cohesive energy upon contact of the NP surfaces, independent of the solvation characteristics of the ligand shells.

In our ongoing work, we will attempt to describe the continuously varying landscape with a more economical implicit ligand model. One possible approach could be the calculation of the FE of the inter-NP approach for a wide range of surface-ligand coverage using an explicit ligand system and incorporation of such a FE into an effective inter-NP potential energy function. In such a scenario, the NP surface beads would encode the specific patchy or directional interactions exhibited by explicit ligands. Another productive direction would be the use of mean-field approximations to model ligand−ligand interactions, typically used for the calculation of interactions between DNA-coated colloids.[46−50] This would allow for a very large reduction in the computational cost of simulating large number of ligand beads and a corresponding increase in the system sizes. It would also be interesting to study the effect, of vastly different solvation qualities of the fluids that make up the fluid−fluid interface, on the self-assembly process. This can be approached by ascribing a different solvent parameter to interactions above (say air, i.e., $s \approx 1$) and below the interface dividing plane (say liquid with $s \ll 1$). This would also involve careful calibration of the imposed PMF of vertical fluctuation on each NP. Additionally, using the simulation protocol described in this work as a base, it would be interesting to explore the other aspects of "ligand engineering", for example, the distinct steric effects of different NP ligand geometries (i.e., linear vs branched) and chain lengths, and how to pre-program the ligands to undergo transitions between different clustering states to steer NPs along target assembly pathways. In a different front, apart from their use as order parameters, the pair-alignment parameters introduced in this work can be used for adding alignment biases in a simulation methodology. This strategy could be used for enforcing specific relative orientations between nearest-neighbor pairs or for implementing force (torque)-based (MD) or energy-based (Monte Carlo) biased-sampling techniques.

■ ASSOCIATED CONTENT

Supporting Information

The Supporting Information is available free of charge at https://pubs.acs.org/doi/10.1021/acs.langmuir.1c02804.

Additional details on the simulation model, methods, and analysis of sample dynamic trajectories (PDF)

New pair-alignment parameter (MP4)

Structural transformations (affine transformation without ligands) (MP4)

Structural transformations (affine transformation with ligands) (MP4)

Structural transformations (serpentine blob) (MP4)

■ AUTHOR INFORMATION

Corresponding Author

F. A. Escobedo − *R. F. Smith School of Chemical and Biomolecular Engineering, Cornell University, Ithaca, New York 14853, United States;* orcid.org/0000-0002-4722-9836; Email: fe13@cornell.edu

Author

U. Gupta − *R. F. Smith School of Chemical and Biomolecular Engineering, Cornell University, Ithaca, New York 14853, United States*

Complete contact information is available at: https://pubs.acs.org/10.1021/acs.langmuir.1c02804

https://doi.org/10.1021/acs.langmuir.1c02804
Langmuir 2022, 38, 1738−1747

Notes

The authors declare no competing financial interest.

■ ACKNOWLEDGMENTS

The authors acknowledge funding support from the NSF Grant CBET-1803878. This work used the Extreme Science and Engineering Discovery Environment (XSEDE), which is supported by the National Science Foundation grant number ACI-1053575. The authors are grateful to Prof. T. Hanrath and Dr. Daniel Balazs for helpful discussions.

■ ABBREVIATIONS

NP, nanoparticle; FE, free energy; PMF, potential-of-mean-force; QOCO, quaternion-based orientation constraint; CO, cuboctahedron; TO, truncated octahedron; US, umbrella sampling; LJ, Lennard-Jones; NN, nearest neighbors

■ REFERENCES

(1) Kovalenko, M. V.; Manna, L.; Cabot, A.; Hens, Z.; Talapin, D. V.; Kagan, C. R.; Klimov, V. I.; Rogach, A. L.; Reiss, P.; Milliron, D. J.; Guyot-Sionnnest, P.; Konstantatos, G.; Parak, W. J.; Hyeon, T.; Korgel, B. A.; Murray, C. B.; Heiss, W. Prospects of Nanoscience with Nanocrystals. *ACS Nano* **2015**, *9*, 1012−1057.

(2) Glotzer, S. C.; Solomon, M. J.; Kotov, N. A. Self-Assembly: From Nanoscale to Microscale Colloids. *AIChE J.* **2004**, *50*, 2978−2985.

(3) Balazs, D. M.; Loi, M. A. Lead-Chalcogenide Colloidal-Quantum-Dot Solids: Novel Assembly Methods, Electronic Structure Control, and Application Prospects. *Adv. Mater.* **2018**, *30*, 1800082.

(4) Kagan, C. R.; Lifshitz, E.; Sargent, E. H.; Talapin, D. V. Building Devices from Colloidal Quantum Dots. *Science* **2016**, *353*, aac5523.

(5) Anikeeva, P. O.; Halpert, J. E.; Bawendi, M. G.; Bulović, V. Quantum Dot Light-Emitting Devices with Electroluminescence Tunable over the Entire Visible Spectrum. *Nano Lett.* **2009**, *9*, 2532−2536.

(6) Fang, P.-P.; Chen, S.; Deng, H.; Scanlon, M. D.; Gumy, F.; Lee, H. J.; Momotenko, D.; Amstutz, V.; Cortés-Salazar, F.; Pereira, C. M.; Yang, Z.; Girault, H. H. Conductive Gold Nanoparticle Mirrors at Liquid/Liquid Interfaces. *ACS Nano* **2013**, *7*, 9241−9248.

(7) Mangolini, L.; Thimsen, E.; Kortshagen, U. High-Yield Plasma Synthesis of Luminescent Silicon Nanocrystals. *Nano Lett.* **2005**, *5*, 655−659.

(8) Baxter, J.; Bian, Z.; Chen, G.; Danielson, D.; Dresselhaus, M. S.; Fedorov, A. G.; Fisher, T. S.; Jones, C. W.; Maginn, E.; Kortshagen, U.; Manthiram, A.; Nozik, A.; Rolison, D. R.; Sands, T.; Shi, L.; Sholl, D.; Wu, Y. Nanoscale Design to Enable the Revolution in Renewable Energy. *Energy Environ. Sci.* **2009**, *2*, 559.

(9) Nozik, A. J.; Beard, M. C.; Luther, J. M.; Law, M.; Ellingson, R. J.; Johnson, J. C. Semiconductor Quantum Dots and Quantum Dot Arrays and Applications of Multiple Exciton Generation to Third-Generation Photovoltaic Solar Cells. *Chem. Rev.* **2010**, *110*, 6873−6890.

(10) Talapin, D. V.; Lee, J.-S.; Kovalenko, M. V.; Shevchenko, E. V. Prospects of Colloidal Nanocrystals for Electronic and Optoelectronic Applications. *Chem. Rev.* **2010**, *110*, 389−458.

(11) Evers, W. H.; Goris, B.; Bals, S.; Casavola, M.; de Graaf, J.; van Roij, R.; Dijkstra, M.; Vanmaekelbergh, D. Low-Dimensional Semiconductor Superlattices Formed by Geometric Control over Nanocrystal Attachment. *Nano Lett.* **2013**, *13*, 2317−2323.

(12) Whitham, K.; Yang, J.; Savitzky, B. H.; Kourkoutis, L. F.; Wise, F.; Hanrath, T. Charge Transport and Localization in Atomically Coherent Quantum Dot Solids. *Nat. Mater.* **2016**, *15*, 557−563.

(13) Baumgardner, W. J.; Whitham, K.; Hanrath, T. Confined-but-Connected Quantum Solids via Controlled Ligand Displacement. *Nano Lett.* **2013**, *13*, 3225−3231.

(14) Cho, K.-S.; Talapin, D. V.; Gaschler, W.; Murray, C. B. Designing PbSe Nanowires and Nanorings through Oriented Attachment of Nanoparticles. *J. Am. Chem. Soc.* **2005**, *127*, 7140−7147.

(15) Whitham, K.; Hanrath, T. Formation of Epitaxially Connected Quantum Dot Solids: Nucleation and Coherent Phase Transition. *J. Phys. Chem. Lett.* **2017**, *8*, 2623−2628.

(16) Walravens, W.; De Roo, J.; Drijvers, E.; ten Brinck, S.; Solano, E.; Dendooven, J.; Detavernier, C.; Infante, I.; Hens, Z. Chemically Triggered Formation of Two-Dimensional Epitaxial Quantum Dot Superlattices. *ACS Nano* **2016**, *10*, 6861−6870.

(17) Soligno, G.; Vanmaekelbergh, D. Understanding the Formation of PbSe Honeycomb Superstructures by Dynamics Simulations. *Phys. Rev. X* **2019**, *9*, 021015.

(18) Gupta, U.; Escobedo, F. A. An Implicit-Solvent Model for the Interfacial Configuration of Colloidal Nanoparticles and Application to the Self-Assembly of Truncated Cubes. *J. Chem. Theory Comput.* **2020**, *16*, 5866−5875.

(19) Abelson, A.; Qian, C.; Salk, T.; Luan, Z.; Fu, K.; Zheng, J.-G.; Wardini, J. L.; Law, M. Collective Topo-Epitaxy in the Self-Assembly of a 3D Quantum Dot Superlattice. *Nat. Mater.* **2020**, *19*, 49−55.

(20) Fan, Z.; Grünwald, M. Orientational Order in Self-Assembled Nanocrystal Superlattices. *J. Am. Chem. Soc.* **2019**, *141*, 1980−1988.

(21) Marino, E.; Kodger, T. E.; Wegdam, G. H.; Schall, P. Revealing Driving Forces in Quantum Dot Supercrystal Assembly. *Adv. Mater.* **2018**, *30*, 1803433.

(22) Peters, J. L.; Altantzis, T.; Lobato, I.; Jazi, M. A.; van Overbeek, C.; Bals, S.; Vanmaekelbergh, D.; Sinai, S. B. Mono- and Multilayer Silicene-Type Honeycomb Lattices by Oriented Attachment of PbSe Nanocrystals: Synthesis, Structural Characterization, and Analysis of the Disorder. *Chem. Mater.* **2018**, *30*, 4831−4837.

(23) Savitzky, B. H.; Hovden, R.; Whitham, K.; Yang, J.; Wise, F.; Hanrath, T.; Kourkoutis, L. F. Propagation of Structural Disorder in Epitaxially Connected Quantum Dot Solids from Atomic to Micron Scale. *Nano Lett.* **2016**, *16*, 5714−5718.

(24) Dong, A.; Jiao, Y.; Milliron, D. J. Electronically Coupled Nanocrystal Superlattice Films by *in Situ* Ligand Exchange at the Liquid−Air Interface. *ACS Nano* **2013**, *7*, 10978−10984.

(25) daSilva, J. C.; Smeaton, M. A.; Dunbar, T. A.; Xu, Y.; Balazs, D. M.; Kourkoutis, L. F.; Hanrath, T. Mechanistic Insights into Superlattice Transformation at a Single Nanocrystal Level Using Nanobeam Electron Diffraction. *Nano Lett.* **2020**, *20*, 5267−5274.

(26) Geuchies, J. J.; van Overbeek, C.; Evers, W. H.; Goris, B.; de Backer, A.; Gantapara, A. P.; Rabouw, F. T.; Hilhorst, J.; Peters, J. L.; Konovalov, O.; Petukhov, A. V.; Dijkstra, M.; Siebbeles, L. D. A.; van Aert, S.; Bals, S.; Vanmaekelbergh, D. In Situ Study of the Formation Mechanism of Two-Dimensional Superlattices from PbSe Nanocrystals. *Nat. Mater.* **2016**, *15*, 1248−1254.

(27) Khadilkar, M. R.; Escobedo, F. A. Self-Assembly of Binary Space-Tessellating Compounds. *J. Chem. Phys.* **2012**, *137*, 194907.

(28) Gupta, U.; Hanrath, T.; Escobedo, F. A. Modeling the Orientational and Positional Behavior of Polyhedral Nanoparticles at Fluid-Fluid Interfaces. *Phys. Rev. Mater.* **2017**, *1*, 055602.

(29) Plimpton, S. Fast Parallel Algorithms for Short-Range Molecular Dynamics. *J. Comput. Phys.* **1995**, *117*, 1−19.

(30) Marrink, S. J.; Risselada, H. J.; Yefimov, S.; Tieleman, D. P.; de Vries, A. H. The MARTINI Force Field: Coarse Grained Model for Biomolecular Simulations. *J. Phys. Chem. B* **2007**, *111*, 7812−7824.

(31) Peters, J. L.; van den Bos, K. H. W.; Van Aert, S.; Goris, B.; Bals, S.; Vanmaekelbergh, D. Ligand-Induced Shape Transformation of PbSe Nanocrystals. *Chem. Mater.* **2017**, *29*, 4122−4128.

(32) Bealing, C. R.; Baumgardner, W. J.; Choi, J. J.; Hanrath, T.; Hennig, R. G. Predicting Nanocrystal Shape through Consideration of Surface-Ligand Interactions. *ACS Nano* **2012**, *6*, 2118−2127.

(33) Gissinger, J. R.; Jensen, B. D.; Wise, K. E. Modeling Chemical Reactions in Classical Molecular Dynamics Simulations. *Polymer* **2017**, *128*, 211−217.

(34) Hens, Z.; Martins, J. C. A Solution NMR Toolbox for Characterizing the Surface Chemistry of Colloidal Nanocrystals. *Chem. Mater.* **2013**, *25*, 1211−1221.

(35) Anderson, J. A.; Antonaglia, J.; Millan, J. A.; Engel, M.; Glotzer, S. C. Shape and Symmetry Determine Two-Dimensional Melting Transitions of Hard Regular Polygons. *Phys. Rev. X* **2017**, *7*, 021001.

https://doi.org/10.1021/acs.langmuir.1c02804
Langmuir 2022, 38, 1738−1747

(36) Steinhardt, P. J.; Nelson, D. R.; Ronchetti, M. Bond-Orientational Order in Liquids and Glasses. *Phys. Rev. B: Condens. Matter Mater. Phys.* **1983**, *28*, 784−805.
(37) Torrie, G. M.; Valleau, J. P. Nonphysical Sampling Distributions in Monte Carlo Free-Energy Estimation: Umbrella Sampling. *J. Comput. Phys.* **1977**, *23*, 187−199.
(38) Weidman, M. C.; Smilgies, D.-M.; Tisdale, W. A. Kinetics of the Self-Assembly of Nanocrystal Superlattices Measured by Real-Time in Situ X-Ray Scattering. *Nat. Mater.* **2016**, *15*, 775−781.
(39) Bian, K.; Choi, J. J.; Kaushik, A.; Clancy, P.; Smilgies, D.-M.; Hanrath, T. Shape-Anisotropy Driven Symmetry Transformations in Nanocrystal Superlattice Polymorphs. *ACS Nano* **2011**, *5*, 2815−2823.
(40) Rabani, E.; Reichman, D. R.; Geissler, P. L.; Brus, L. E. Drying-Mediated Self-Assembly of Nanoparticles. *Nature* **2003**, *426*, 271−274.
(41) Zhang, H.; Banfield, J. F. Energy Calculations Predict Nanoparticle Attachment Orientations and Asymmetric Crystal Formation. *J. Phys. Chem. Lett.* **2012**, *3*, 2882−2886.
(42) Chen, I. Y.; Cimada daSilva, J.; Balazs, D. M.; Smeaton, M. A.; Kourkoutis, L. F.; Hanrath, T.; Clancy, P. The Role of Dimer Formation in the Nucleation of Superlattice Transformations and Its Impact on Disorder. *ACS Nano* **2020**, *14*, 11431−11441.
(43) Nishiyama, Z. *Martensitic Transformation*; Elsevier, 2012.
(44) Murray, B. S.; Nelson, P. V. A Novel Langmuir Trough for Equilibrium and Dynamic Measurements on Air−Water and Oil−Water Monolayers. *Langmuir* **1996**, *12*, 5973−5976.
(45) Benjamins, J.; de Feijter, J. A.; Evans, M. T. A.; Graham, D. E.; Phillips, M. C. Dynamic and Static Properties of Proteins Adsorbed at the Air/Water Interface. *Faraday Discuss. Chem. Soc.* **1975**, *59*, 218.
(46) Varilly, P.; Angioletti-Uberti, S.; Mognetti, B. M.; Frenkel, D. A General Theory of DNA-Mediated and Other Valence-Limited Colloidal Interactions. *J. Chem. Phys.* **2012**, *137*, 094108.
(47) Angioletti-Uberti, S.; Varilly, P.; Mognetti, B. M.; Tkachenko, A. V.; Frenkel, D. Communication: A simple analytical formula for the free energy of ligand-receptor-mediated interactions. *J. Chem. Phys.* **2013**, *138*, 021102.
(48) Angioletti-Uberti, S.; Varilly, P.; Mognetti, B. M.; Frenkel, D. Mobile Linkers on DNA-Coated Colloids: Valency without Patches. *Phys. Rev. Lett.* **2014**, *113*, 128303.
(49) Hu, H.; Ruiz, P. S.; Ni, R. Entropy Stabilizes Floppy Crystals of Mobile DNA-Coated Colloids. *Phys. Rev. Lett.* **2018**, *120*, 048003.
(50) Rogers, W. B. A mean-field model of linker-mediated colloidal interactions. *J. Chem. Phys.* **2020**, *153*, 124901.

https://doi.org/10.1021/acs.langmuir.1c02804
Langmuir 2022, 38, 1738−1747